Coherent Integration for Radar High-Speed Maneuvering Target Based on Frequency-Domain Second-Order Phase Difference

Ke Jin [1],* , **Tao Lai [1]**, **Yubing Wang [2]**, **Gongquan Li [1]** and **Yongjun Zhao [1]**

[1] National Digital Switching System Engineering and Technological Research Center, Zhengzhou 450000, China; ltnudt@126.com (T.L.); lgq1225@126.com (G.L.); zhaoyjzz@163.com (Y.Z.)

[2] Air Traffic Control and Navigation College, Air Force Engineering University, Xi'an 710000, China; wangyubing_AFU@126.com

* Correspondence: jinke_xd@outlook.com

Abstract: In recent years, target detection has drawn increasing attention in the field of radar signal processing. In this paper, we address the problem of coherent integration for detecting high-speed maneuvering targets, involving range migration (RM), quadratic RM (QRM), and Doppler frequency migration (DFM) within the coherent processing interval. We propose a novel coherent integration algorithm based on the frequency-domain second-order phase difference (FD-SoPD) approach. First, we use the FD-SoPD operation to reduce the signal from three to two dimensions and simultaneously eliminate the effects of QRM and DFM, which leads to signal-to-noise ratio improvement in the velocity-acceleration domain. Next, we estimate the target motion parameters from the peak position without the need for a search procedure. We show that this algorithm can be easily implemented by using complex multiplications combined with fast Fourier transform (FFT) and inverse FFT (IFFT) operations. We perform comparisons with several representative algorithms and show that the proposed technique can be used to achieve a good trade-off between computational complexity and detection performance. We present both simulated and experimental data to demonstrate the effectiveness of the proposed method.

1. Introduction

With the increasing requirements for space target detection and high-resolution imaging, radar high-speed maneuvering target detection has drawn growing attention [1–11]. Normally, a low-speed target is located in the same range cell during the short observation time, and the conventional moving target detection (MTD) algorithm [12] can complete coherent integration by using fast Fourier transform (FFT). It is well known that in order to improve the detection ability in far-range and low radar cross section (RCS) targets, a long-term coherent integration is always required [13]. In this case, for high-speed maneuvering targets, the linear range migration (LRM), quadratic range migration (QRM), and Doppler frequency migration (DFM) effects will inevitably occur, thereby deteriorating integration performance.

As for radar coherent integration, many successful detection algorithms have been proposed, such as the keystone transform (KT) [14,15], scaled inverse Fourier transform (SCIFT) [16,17], frequency-domain deramp-keystone transform (FDDKT) [18], modified location rotation transform (MLRT) [19], and Radon Fourier transform (RFT) [20]. For a moving target with linear range migration, these algorithms achieve satisfactory antinoise performance, parameter estimation accuracy,

and detection ability with reasonable computational cost. Nevertheless, they may suffer from integration performance degradation due to ignoring the effects of QRM and DFM caused by the target's acceleration.

To address these issues, many advanced methods have been recently proposed. They can be roughly divided into three categories.

(a)   Radon transform-based algorithms, such as generalized Radon Fourier transform (GRFT) [21], Radon-fractional Fourier transform (RFRFT) [22], and Radon-Lv's Distribution (RLVD) [23–26]. These kinds of algorithms implement phase compensation and parameter estimation by searching the maneuvering target motion trajectory. Although they can obtain coherent integration under a low signal-to-noise ratio (SNR), the huge computational load seriously limits their practical application.

(b)   KT based algorithms, such as second-order keystone transform (SoKT) [27], Doppler keystone transform (DKT) [28], keystone-Lv's distribution (KT-LVD) [29], and so on. The KT is used to correct the QRM blindly, which reduces the calculation cost to a certain extent, but it still needs to use parameter searching to eliminate the Doppler ambiguity.

(c)   Correlation-based algorithms: The representative adjacent cross-correlation function and Lv's distribution (ACCF-LVD) algorithm proposed in References [30–32] reduces the migration order by ACCF and quickly estimates the motion parameters without any searching procedure, which greatly reduces the computational burden and benefits practical applications. Unfortunately, this method is only effective when the input SNR is high [33]. The three-dimensional scaled transform (TDST) method was then presented to realize coherent integration and motion parameters estimations for maneuvering targets under a low SNR background [34]. This method eliminates the coupling effectively among spatial frequency, slow time, and time delay. However, the complex three-dimensional transform is usually less suitable for realistic applications.

Aiming to realize the coherent integration of radar high-speed maneuvering targets with low computational complexity, we propose a novel frequency-domain second-order phase difference (FD-SoPD) algorithm in this paper. First, the SoPD is used in the spatial frequency domain to eliminate the impact of acceleration. Then, we can simultaneously estimate the velocity and acceleration from the peak position, followed by phase compensation and coherent integration. The proposed technique has the following contributions: (a) It reduces the signal from three to two dimensions, thus avoiding the complex operation of TDST; (b) the target motion parameters can be easily estimated by FFT without any searching process; (c) the phase difference eliminates the Doppler ambiguity, thus the high speed of target can be accurately estimated; (d) it achieves a good balance between the computational cost and detection ability. Finally, we present both simulated and experimental data to demonstrate the effectiveness of the proposed method.

The remainder of this paper is organized as follows. In Section 2, the signal model for the maneuvering target is established. In Section 3, we deduce the principle of FD-SoPD in detail and discuss the situations of single target and multi-targets, respectively. Section 4 analyses the computational burden. In Section 5, we evaluate the performance via several numerical experiments. Finally, conclusions are drawn in Section 6.

2. Signal Model and Problem Formulation

Suppose the radar transmits a linear frequency modulated (LFM) signal, which can be expressed as:

$$s_t(\hat{t}) = \mathrm{rect}\left(\frac{\hat{t}}{T_p}\right) \exp\left(j2\pi f_c\hat{t} + j\pi\gamma\hat{t}^2\right) \qquad (1)$$

where,

$$\text{rect}\left(\frac{\hat{t}}{T_p}\right) = \begin{cases} 1, & |\hat{t}| < T_p/2 \\ 0, & |\hat{t}| > T_p/2 \end{cases} \tag{2}$$

is the rectangular window function, and $\hat{t}$ is the fast time. T_p, f_c and γ indicate the pulse width, carrier frequency, and frequency modulation rate, respectively. Assume that there are K targets in the scene of radar observation. During the accumulation time, the distance between the maneuvering target and radar can be approximated as second order, i.e.,

$$R_i(t_m) = r_i + v_i t_m + a_i t_m^2/2 \tag{3}$$

where $t_m = m/PRF$ is the slow time, m and PRF denote the transmitted pulse number index and the pulse repetition frequency (PRF). r_i, v_i, and a_i are respectively the initial slant range, radial velocity, and acceleration of the ith target.

Ignoring the influence of noise, the received signal of K targets after down conversion can be expressed as [35]:

$$s_r(\hat{t}, t_m) = \sum_{i=1}^{K} A_{r,i} \text{rect}\left(\frac{\hat{t} - 2R_i(t_m)/c}{T_p}\right) \exp\left\{-j\frac{4\pi f_c R_i(t_m)}{c}\right\} \exp\left\{j\pi\gamma\left(\hat{t} - \frac{2R_i(t_m)}{c}\right)^2\right\} \tag{4}$$

where $A_{r,i}$ is the target reflectivity, and c is the light speed.

After pulse compression, the radar echoes are written as:

$$s_c(\hat{t}, t_m) = \sum_{i=1}^{K} A_{c,i} \text{sinc}\left[B\left(\hat{t} - \frac{2R_i(t_m)}{c}\right)\right] \exp\left\{-j\frac{4\pi f_c R_i(t_m)}{c}\right\} \tag{5}$$

where $A_{c,i}$ denotes the amplitude after compression and $B = \gamma T_p$ is the bandwidth of transmitted signal.

Substituting Equation (3) into Equation (5), we obtain:

$$s_c(\hat{t}, t_m) = \sum_{i=1}^{K} A_{c,i} \text{sinc}\left[B\left(\hat{t} - \frac{2(r_i + v_i t_m + a_i t_m^2/2)}{c}\right)\right] \exp\left\{-j\frac{4\pi f_c(r_i + v_i t_m + a_i t_m^2/2)}{c}\right\} \tag{6}$$

As can be seen from Equation (6), the signal envelope indicates the target range, which changes nonlinearly with the slow time. When the offset exceeds the range resolution $\Delta r = c/2B$, the LRM will occur. If the target has a large acceleration, the QRM can be seen in the envelope. In this case, the conventional MTD is invalid. In addition, the phase in Equation (6) indicates a linear change in the Doppler frequency of the ith target, i.e.,

$$f_{d,i} = \frac{2}{\lambda}\frac{\text{d}\left(r_i + v_i t_m + a_i t_m^2/2\right)}{\text{d}t_m} = \frac{2v_i + 2a_i t_m}{\lambda} \tag{7}$$

where $\lambda = c/f_c$ is the wave length. Similarly, when the offset exceeds a Doppler resolution, DFM would occur and defocus the target energy in the Doppler domain. Moreover, for high-speed targets, we often have $f_{d,i} \gg PRF$, which induces the Doppler ambiguity and makes it hard to estimate the target's velocity. Therefore, the coherent accumulation of high-speed maneuvering targets can only be achieved by effectively eliminating the LRM, QRM, and DFM.

3. The Principle of the FD-SoPD

3.1. FD-SoPD with Mono-Target

According to Equation (6), the compressed signal of the ith target is

$$s_c(\hat{t}, t_m) = A_{c,i}\text{sinc}\left[B\left(\hat{t} - \frac{2\left(r_i + v_i t_m + a_i t_m^2/2\right)}{c}\right)\right]\exp\left\{-j\frac{4\pi f_c\left(r_i + v_i t_m + a_i t_m^2/2\right)}{c}\right\} \quad (8)$$

Performing the Fourier transform (FT) along the $\hat{t}$ axis, we obtain the spatial spectrum of the signal, i.e.,

$$\begin{aligned} S(f_r, t_m) &= A_{f_r,i}\text{rect}\left(\frac{f_r}{B}\right)\exp\left(-j\frac{4\pi(f_r+f_c)R_i(t_m)}{c}\right) \\ &= A_{f_r,i}\text{rect}\left(\frac{f_r}{B}\right)\exp\left\{-j4\pi\frac{(f_r+f_c)}{c}\left(r_i + v_i t_m + a_i t_m^2/2\right)\right\} \end{aligned} \quad (9)$$

where f_r is the frequency of the spatial harmonic from the spatial spectrum of the fast time signal record, and $A_{f_r,i}$ is the amplitude of the spatial harmonic obtained by FT of the fast time signal record.

As shown in Equation (9), the coupling between f_r and t_m (or t_m^2) is the fundamental cause of LRM or QRM. Moreover, the existence of t_m^2 broadens the Doppler spectrum and makes the signal energy defocused. If the velocity v_i and acceleration a_i are accurately estimated, it is easy to perform phase compensation and coherent integration.

The proposed FD-SoPD is defined as:

$$R_{SoPD}(t_m, \tau, \tau_1; f_r) = S\left(f_r; t_m + \frac{\tau}{2}\right)S^*\left(f_r; t_m - \frac{\tau}{2}\right)\left[S\left(f_r; t_m + \frac{\tau_1}{2}\right)S^*\left(f_r; t_m - \frac{\tau_1}{2}\right)\right]^* \quad (10)$$

where τ and τ_1 are two lag time variables. Substituting Equation (9) into Equation (10) yields:

$$\begin{aligned} R_{SoPD}(f_r, t_m, \tau; \tau_0) &= \left|A_{f_r,i}\right|^4\text{rect}\left(\frac{f_r}{B}\right)\exp\left[j4\pi\frac{f_r+f_c}{c}v_i(\tau_1 - \tau)\right] \\ &\times \exp\left[j4\pi\frac{f_r+f_c}{c}a_i t_m(\tau_1 - \tau)\right] \end{aligned} \quad (11)$$

When τ and τ_1 have fixed nonzero lag time difference, the coupling between τ and τ_1 will be eliminated, i.e.,

$$2\tau_0 = \tau_1 - \tau \quad (12)$$

where τ_0 is the fixed lag time. Equation (11) can be further expressed as:

$$\begin{aligned} R_{SoPD}(f_r, t_m, \tau; \tau_0) &= \left|A_{f_r,i}\right|^4\text{rect}\left(\frac{f_r}{B}\right)\exp\left(j8\pi\frac{f_r+f_c}{c}v_i\tau_0\right) \\ &\times \exp\left(j8\pi\frac{f_r+f_c}{c}a_i\tau_0 t_m\right) \end{aligned} \quad (13)$$

As shown in Equation (13), three axes, f_r, t_m and τ, exist in $R_{SoPD}(f_r, t_m, \tau; \tau_0)$. However, the signal energy is constant along the τ axis, and thus can be accumulated coherently by the addition operation as follows:

$$\begin{aligned} R_A(f_r, t_m; \tau_0) &= \text{ADD}_\tau[R_{SoPD}(f_r, t_m, \tau; \tau_0)] \\ &= G_m\left|A_{f_r,i}\right|^4\text{rect}\left(\frac{f_r}{B}\right)\exp\left(j8\pi\frac{f_r+f_c}{c}v_i\tau_0\right)\exp\left(j8\pi\frac{f_r+f_c}{c}a_i\tau_0 t_m\right) \end{aligned} \quad (14)$$

where $\text{ADD}_\tau(\cdot)$ is the addition function along the τ axis and G_m denotes the corresponding integration gain.

Remark 1. *From Equation (14), we may find three features of the FD-SoPD. (a) The signal is reduced from three to two dimensions, which avoids the multidimensional scaled transform in TDST algorithm. (b) The QRM and*

DRM are simultaneously eliminated. (c) Equation (14) is equivalent to a uniform motion model, whose velocity is $-2a_i\tau_0$. Thus, the Doppler ambiguity is eliminated. If the envelope migration caused by the velocity $-2a_i\tau_0$ exceeds a range cell, the KT is needed, i.e.,

$$(f_r + f_c)t_m = f_c\tau_m \tag{15}$$

where τ_m denotes the scaled slow-time variable.

After performing the KT on Equation (14), we have:

$$R_A(f_r, \tau_m; \tau_0) = G_m\left|A_{f_r,i}\right|^4 rect\left(\frac{f_r}{B}\right)\exp\left(j8\pi\frac{f_c}{c}v_i\tau_0\right)$$
$$\times \exp\left(j8\pi\frac{f_r}{c}v_i\tau_0\right)\exp\left(j8\pi\frac{f_c}{c}a_i\tau_0\tau_m\right) \tag{16}$$

Applying the FT with respect to f_r and τ_m, we get:

$$S_F\left(\hat{t}, f_{\tau m}\right) = FT_{\tau_m}\left\{FT_{f_r}[R_A(f_r, \tau_m; \tau_0)]\right\}$$
$$= A_{F,i}\exp\left(j\frac{8\pi f_c v_i\tau_0}{c}\right)\text{sinc}\left[B\left(\hat{t}+\frac{4v_i\tau_0}{c}\right)\right]\text{sinc}\left[CI\left(f_{\tau m}-\frac{4a_i\tau_0}{\lambda}\right)\right] \tag{17}$$

where $A_{F,i}$ is amplitude after two-dimensional FT, $f_{\tau m}$ is the frequency with respect to τ_m, and CI denotes the coherent integration time.

From Equation (17), we can simultaneously estimate the velocity v_i and acceleration a_i of the ith target, i.e.,

$$\left(\hat{v}_i = \frac{-c\hat{t}_{\max}}{4\tau_0}, \hat{a}_i = \frac{\lambda f_{\tau m,\max}}{4\tau_0}\right) \tag{18}$$

Notice that the fixed lag time constant τ_0 is important in the implementation of the SoPD. A large fixed lag time τ_0 will improve the parameter estimation accuracy, whereas spectrum aliasing may occur. Therefore, the compromise consideration usually chooses $\tau_0 < T_a/4$, where T_a is the observation time.

Utilizing the estimated parameters, we can construct the phase compensation function to compensate the LRM, QRM, and DFM in Equation (9)

$$H_{com}(f_r, t_m) = \exp\left(j4\pi f_r\frac{v_i t_m + a_i t_m^2/2}{c}\right)\exp\left(j4\pi f_c\frac{a_i t_m^2/2}{c}\right) \tag{19}$$

Finally, the signal energy will be integrated by the IFT and the FT operations,

$$E\left(\hat{t}, f_d\right) = FT_{t_m}\left\{IFT_{f_r}[S(f_r, t_m)H_{com}(f_r, t_m)]\right\}$$
$$= A_{E,i}\text{sinc}\left[B\left(\hat{t}-\frac{2r_i}{c}\right)\right]\delta(f_d + f_{d0,i}) \tag{20}$$

where f_d is the Doppler frequency with respect to t_m, and $f_{d0,i}$ is the Doppler frequency of the target.

In Equation (20), the signal energy of a high-speed maneuvering target is integrated into a single peak in the range-Doppler domain. The peak position is $(2r_i/c, -f_{d0,i})$ and the peak value is $\left|E(2r_i/c, -f_{d0,i})\right|$. Here, the constant false alarm rate (CFAR) [36] technique can be used for the target detection, i.e.,

$$\left|E(2r_i/c, -f_{d0,i})\right| \underset{H_0}{\overset{H_1}{\gtrless}} \eta \tag{21}$$

where η is the CFAR threshold. If $\left|E(2r_i/c, -f_{d0,i})\right|$ is larger than the threshold, there will be a moving target. Otherwise, no target is detected.

Remark 2. *Different from the Radon transform based algorithms in [13,21–23], the proposed FD-SoPD method avoids the brute-force searching procedure of unknown motion parameters. In addition, it can be easily implemented by FFT and IFFT, which significantly reduces the computational complexity.*

In the following, we will give an example to demonstrate how the FD-SoPD works to accomplish target motion parameter estimation and coherent integration.

Example 1. *We use an ideal maneuvering point target in this example. The parameters of frequency-modulated continuous-wave (FMCW) radar are set as: The carrier frequency $f_c = 1\,GHz$, the bandwidth $B = 100\,MHz$, the sampling frequency $f_s = 2\,MHz$, pulse repetition frequency $PRF = 128\,Hz$, and the number of integration pulses $M = 256$ and $\tau_0 = T_a/5$. The motion parameters of the maneuvering point target are: $A_{r,i} = 1$, $r_i = 3km$, $v_i = 15\,m/s$, $a_i = 1m/s^2$. Simulation results are shown in Figure 1.*
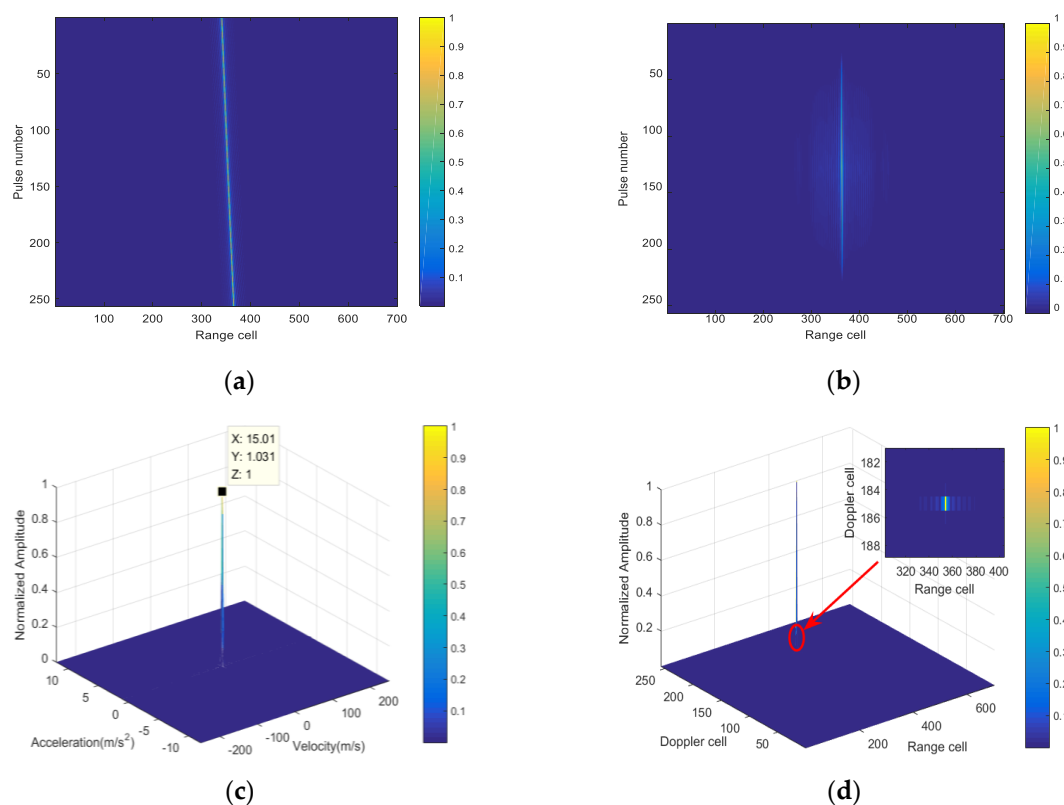
Figure 1. Simulation results of Example 1. (**a**) The result of pulse compression; (**b**) the result of the frequency-domain second-order phase difference (FD-SoPD); (**c**) velocity–acceleration distribution; (**d**) the result of coherent integration.

Figure 1a shows the result of pulse compression, where serious LRM occurs due to the target's high speed and the radar's high resolution. Figure 1b shows the result of FD-SoPD transform. It is obvious that, after the FD-SoPD with respect to slow time, the envelope migration is effectively eliminated, and the target energy is located in the same range cell. Performing the FT with respect to τ_m, we can get the velocity-acceleration distribution, as shown in Figure 1c. The target energy is well accumulated as one peak, and we can estimate $\hat{v}_i = 15.01\,m/s$ and $\hat{a}_i = 1.031m/s^2$ from its position. Finally, coherent integration is easily accomplished with FFT, and the result is given in Figure 1d.

3.2. FD-SoPD with Multi-Targets

In this subsection, we will analyze the performance of FD-SoPD under multi-targets in detail. Assume that there are *K* maneuvering targets in the scene of radar observation. The compressed signal can be expressed as Equation (6). Accordingly, the signal in the spatial frequency domain is:

$$
\begin{aligned}
S(f_r, t_m) &= \sum_{i=1}^{K} A_{f_r,i} rect\left(\frac{f_r}{B}\right) \exp\left(-j\frac{4\pi(f_r+f_c)R_i(t_m)}{c}\right) \\
&= \sum_{i=1}^{K} A_{f_r,i} rect\left(\frac{f_r}{B}\right) \exp\left\{-j4\pi\frac{(f_r+f_c)}{c}\left(r_i + v_i t_m + a_i t_m^2/2\right)\right\}
\end{aligned}
\tag{22}
$$

Substituting Equation (22) into Equation (10) along the slow time, we obtain the FD-SoPD of $S(f_r, t_m)$

$$
R_{SoPD}(f_r, t_m, \tau; \tau_0) = R_{auto}(f_r, t_m, \tau; \tau_0) + R_{cross}(f_r, t_m, \tau; \tau_0)
\tag{23}
$$

where $R_{auto}(f_r, t_m, \tau; \tau_0)$ and $R_{cross}(f_r, t_m, \tau; \tau_0)$ denote the auto-terms and cross terms, and can be written as

$$
\begin{aligned}
R_{auto}(f_r, t_m, \tau; \tau_0) &= \sum_{i=1}^{K} \left|A_{f_r,i}\right|^4 rect\left(\frac{f_r}{B}\right) \exp\left(j8\pi\frac{f_r+f_c}{c}v_i\tau_0\right) \\
&\times \exp\left(j8\pi\frac{f_r+f_c}{c}a_i\tau_0 t_m\right)
\end{aligned}
\tag{24}
$$

$$
R_{cross}(f_r, t_m, \tau; \tau_0) = R_2 + R_3 + R_4 + R_5
\tag{25}
$$

The summation R_5 can be further expanded as the following three parts:

$$
R_5 = R_6 + R_7 + R_8
\tag{26}
$$

The detailed expressions of $R_i(i = 2, 3 \cdots, 8)$ are given in the Appendix A.

After the addition, KT and two-dimensional FT, the velocity and acceleration of target will be estimated simultaneously, i.e.,

$$
S_F(\hat{t}, f_{\tau m}) = \text{FT}_{\tau_m}\left\{\text{FT}_{f_r}\left\{\text{KT}\{\text{ADD}_\tau[R_{SoPD}(f_r, t_m, \tau; \tau_0)]\}\right\}\right\}
\tag{27}
$$

According to the specific motion of the maneuvering target, we consider the cross-terms resulting from the following two cases.

Case 1. *The acceleration of any two targets is different, i.e., $a_i \neq a_j, \forall i, j = 1, 2, \ldots, K, i \neq j$. In this case, R_{auto} has a similar form with Equation (13), which can be integrated after FFT. R_2 has the linear term of τ and the coupling term between t_m and τ, which cannot be accumulated in the addition operation and FFT of Equation (27). R_3, R_4, R_7 and R_8 have the quadratic term τ^2 and a coupling term between t_m and τ, and thus cannot be accumulated as well. It is known from Equation (34) that R_6 has a symmetric property about τ, which will become a sinusoidal oscillation term after the addition in Equation (27). Therefore, the energy of R_6 will be smeared after performing two-dimensional FFT. In summary, the cross terms can be ignored compared to the auto-terms. Here, we give an example to illustrate the discussion of Case 1.*

Example 2. *In this example, we use two maneuvering targets designated as Tr1 and Tr2, respectively. Radar parameters are the same as those in Example 1. Target motion parameters are set as: $A_{r,1} = 1$, $r_1 = 3km$, $v_1 = 15\,m/s$, $a_1 = 1m/s^2$ for target Tr1; $A_{r,2} = 1$, $r_2 = 3.2km$, $v_2 = -12\,m/s$, $a_2 = -0.6m/s^2$ for target Tr2.*

Figure 2a is the result of pulse compression. Figure 2b gives the result of FD-SoPD. It is obvious that the auto-terms are corrected into beelines, while the cross-terms cannot be corrected. Thus, after the addition and two-dimensional FT, only the auto-terms are accumulated into two peaks, as shown in Figure 2c. We can estimate the velocity and acceleration of targets as $\hat{v}_1 = 15.01\,\text{m/s}$, $\hat{a}_1 = 1.067\text{m/s}^2$,

$\hat{v}_2 = -12\,\text{m/s}$, $\hat{a}_2 = -0.5822\text{m/s}^2$. After compensating the RM, QRM, and DFM with the estimated motion parameters, these two targets are coherently integrated, as shown in Figure 2d,e.

(a)

(b)

(c)

(d)

(e)
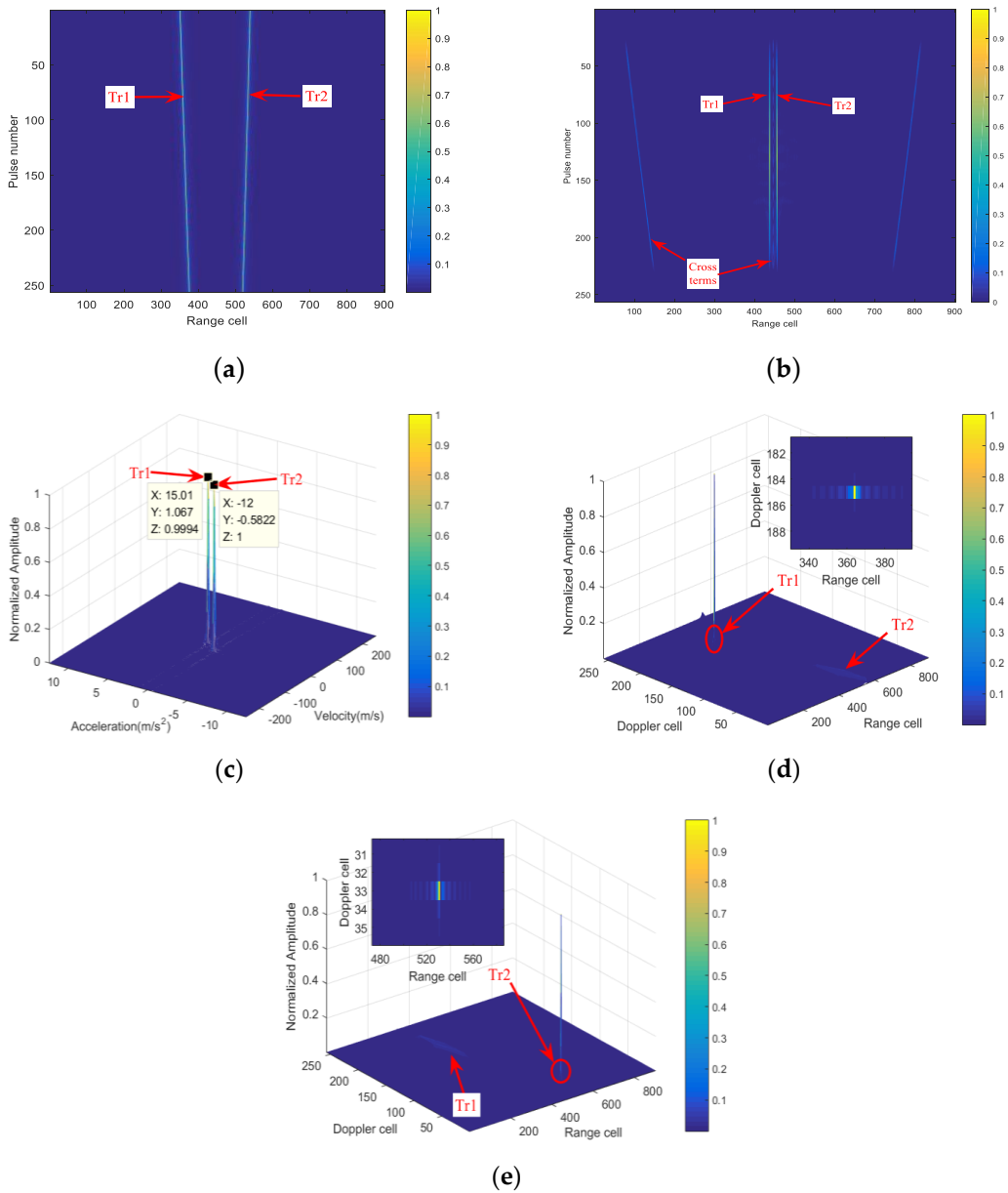
Figure 2. Simulation results of Example 2. (**a**) The result of pulse compression; (**b**) the result of FD-SoPD; (**c**) the velocity-Acceleration distribution; (**d**) coherent integration result of Tr1; (**e**) coherent integration result of Tr2.

Case 2. *Some of the accelerations coincide, i.e., $a_i = a_j$ or $c_{i2} = c_{j2}$, $\exists i, j = 1, 2, \ldots, K$, $i \neq j$. In this case, the coupling term between t_m and τ in R_2 is eliminated, but there are still linear terms of τ. The energy of R_2 will be accumulated only when $c_{i1} = c_{j1}$, which means the two targets have the same velocity and acceleration. i.e., $R_1 = R_2$. R_3, R_4 and R_8 have the quadratic term τ^2 and coupling term between t_m and τ, and thus cannot be accumulated. R_7 has linear terms of τ and a random initial phase regarding target reflectivity and the initial range, which defocuses the target energy.*

As for R_6, when $c_{i2} = c_{j2}$, it can be simplified as:

$$R_6 = \sum_{\substack{i=1 \\ i \neq j}}^{K} \sum_{j=1}^{K} |A_i|^2 |A_j|^2 \exp\left\{j\frac{4\pi}{\varepsilon}\left[(c_{i1} + c_{j1})\tau_0 + 4c_{i2}\tau_0 t_m\right]\right\} \tag{28}$$

Substituting Equation (28) into Equation (27), we can see that R_6 can achieve energy accumulation, and the peak position is in the middle of the auto-terms, that is, the acceleration is the same as the real value, while the velocity is estimated as the average of the two targets.

Example 3. *In this example, two maneuvering targets designated as Tr1 and Tr2 have the same acceleration. Radar parameters are the same as those in Example 1. Target motion parameters are set as: $A_{r,1} = 1$, $r_1 = 2.9km$, $v_1 = 15\,m/s$, $a_1 = 1m/s^2$ for Target Tr1; $A_{r,2} = 1$, $r_2 = 3.1km$, $v_2 = -15\,m/s$, $a_2 = 1m/s^2$ for target Tr2.*

Figure 3a shows the target trajectories after pulse compression. Figure 3b is the result of FD-SoPD. It is obvious that, in addition to the auto-terms, the cross term R_6 is also corrected as a beeline, which locates in the middle of them. Thus, the energy of R_6 is accumulated into Peak 1 in Figure 3c, and the auto-terms form Peak 2 and Peak 3. Moreover, the motion parameters of Peak 1 also confirm the theoretical analysis in Case 2.
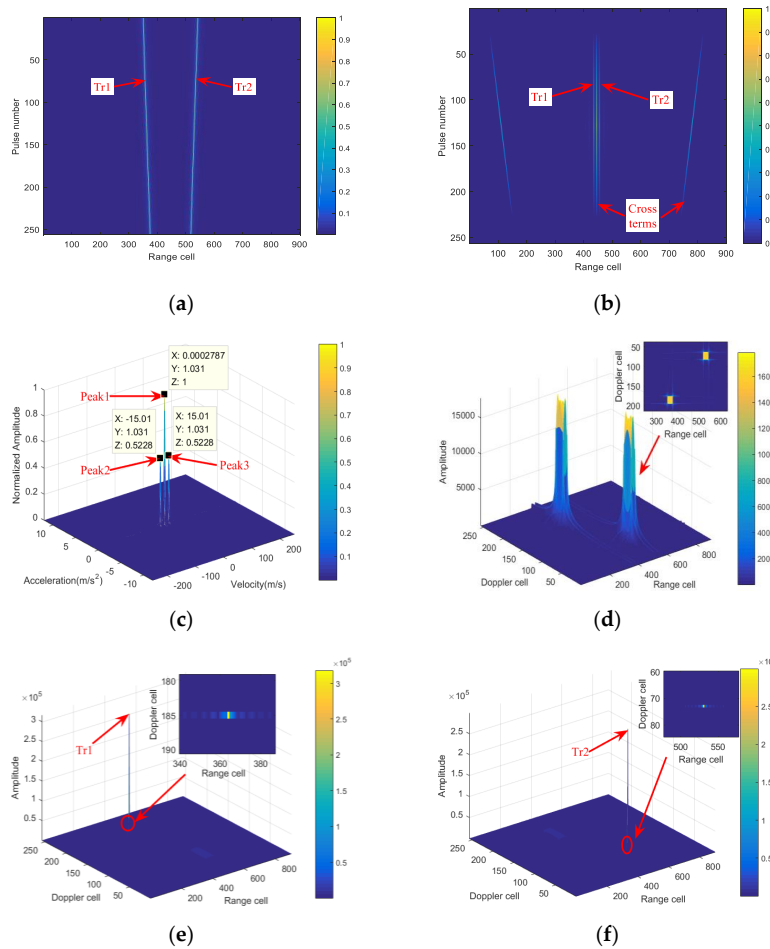
Figure 3. Simulation results of Example 3; (**a**) the result of pulse compression; (**b**) the result of the FD-SoPD; (**c**) the velocity-Acceleration distribution; (**d**) the coherent integration result with peak 1; (**e**) Coherent integration result with peak 2; (**f**) the coherent integration result with peak 3.

The next step is to determine whether all of these peaks are real maneuvering targets. After phase compensation with Peak 1, the coherent integration result is shown in Figure 3d, where no target will be detected by CFAR detection. Therefore, Peak 1 belongs to a cross-term peak. In contrast, integration with Peak 2 or Peak 3 can both produce a single sharp peak in the range-Doppler domain. Thus, Peak 2 and Peak 3 belong to the auto-term peaks. This also provides us with a method for estimating the target motion parameters combined with CFAR detection. The detailed flowchart of the FD-SoPD algorithm is given in Figure 4.
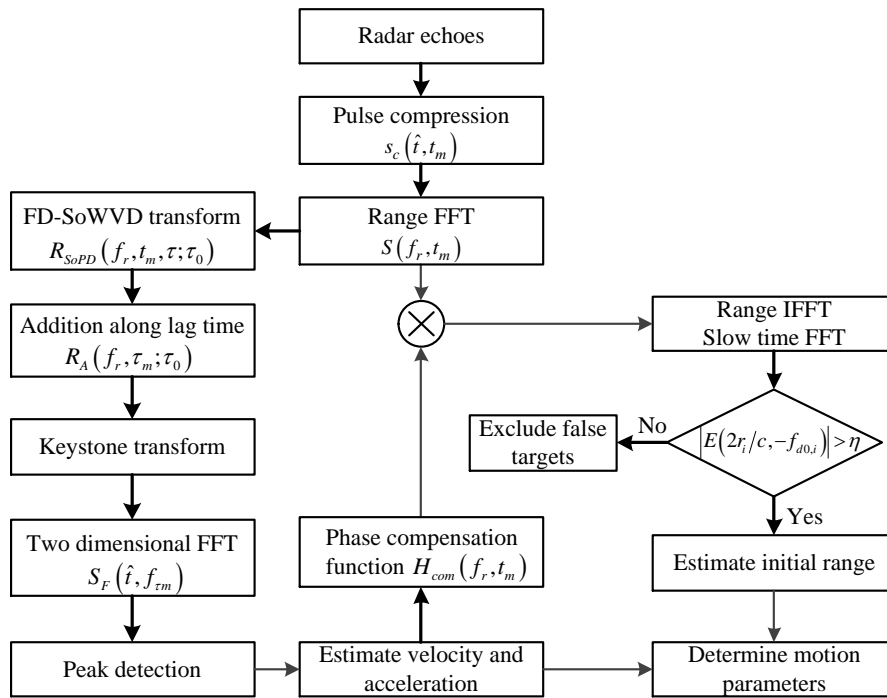
Figure 4. Flowchart of the proposed coherent detection algorithm.

4. Computational Burden Analysis of the FD-SoPD Algorithm

In this section, we will analyze the computational burden of the algorithm. The SCIFT [16], TDST [34], and ACCF-LVD [30] are selected for comparisons.

We denote the number of range cells and pulses by N_r and M. For SCIFT, its main procedures include the symmetric autocorrelation function ($O(2N_r M \log_2 M)$), the chirp-z based SCIFT ($O(3MN_r \log N_r)$), and FFT along the lag time axis ($O(N_r M \log_2 M)$). Therefore, the computational complexity is about $O(3MN_r(\log_2 M + \log N_r))$.

For TDST, to complete the two steps of scaled Fourier transform (SCFT), the computational complexities are $O(3N_r M^2 \log_2 M)$ and $O(3M^2 N_r \log_2 N_r)$, respectively. Thus, the total computational complexity is in the order of $O(3N_r M^2 \log_2 N_r M)$.

For ACCF-LVD, its main procedures include ACCF operation ($O(2MN_r \log_2 N_r)$) and chirp-z based LVD algorithm ($O(3M^2 \log_2 M)$). Therefore, its computational cost is about $O(2MN_r \log_2 N_r + 3M^2 \log_2 M)$.

The implementation of the proposed algorithm needs the calculation of $R_{SoPD}(f_r, t_m, \tau; \tau_0)$ ($O(2M^2 N_r)$), chirp-z based KT ($O(3N_r M \log_2 M)$), and two dimensional FFT ($O(MN_r(\log_2 N_r + \log_2 M))$). Therefore, the overall computational cost of the proposed method is in the order of $O(2M^2 N_r)$.

The computational complexities are listed in Table 1. Under the assumption of $N_r = M$, Figure 5 shows the computational complexities of the above four methods. Obviously, the TDST takes too much time and is not suitable for real-time processing. Table 1 also gives the detailed values

of computational resources. The TDST takes up much more memory to store the three-dimensional matrix [34]. In comparison, the SCIFT, ACCF-LVD, and FD-SoPD show great advantages in this aspect. Therefore, we could conclude that the proposed FD-SoPD cost moderates computational time and resources, which helps practical applications.

Table 1. The computational burden comparisons of different algorithms.

Method	Computational Complexity	Time Cost (s) [1]	Computational Resources
SCIFT	$O(3MN_r(\log_2 M + \log N_r))$	6.35	$O(2MN_r)$
TDST	$O(3N_rM^2\log_2 N_rM)$	335.43	$O(2M^2N_r)$
ACCF-LVD	$O(2MN_r\log_2 N_r + 3M^2\log_2 M)$	6.06	$O(MN_r)$
FD-SoPD	$O(2M^2N_r)$	12.24	$O(MN_r)$

[1] The main configuration of the computer. CPU: Intel Core i7-6700HQ 2.60 GHz; RAM: 16.00G; Operating System: Windows 7; Software: Matlab 2015a.
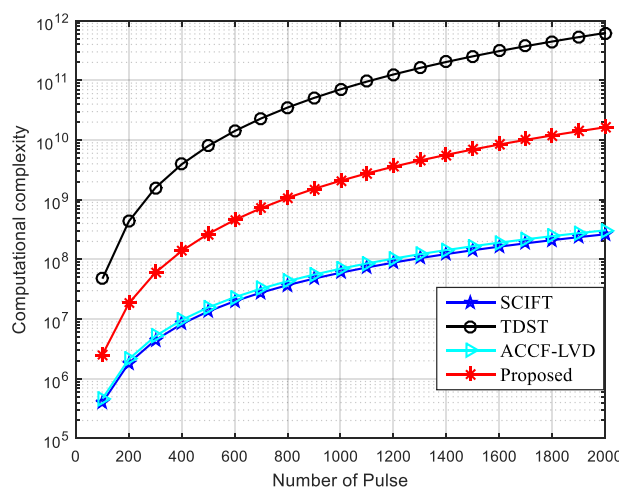
Figure 5. Computational complexity comparison.

5. Numerical Results

In the section, we will give several numerical experiments to demonstrate the effectiveness of the proposed algorithm. The simulation parameters are given in Table 2.

Table 2. Simulation parameters for the radar and target.

Parameters	Value	Parameters	Value
Carrier frequency	1 GHz	Bandwidth	100 MHz
Sample frequency	2 MHz	PRF	128 Hz
Pulse duration	2 ms	Pulse number	256
Initial slant range	3 km	Radial velocity	15 m/s
Radial acceleration	1 m/s^2	-	-

5.1. Coherent Integration Performance

In this part, the coherent integration performance of the proposed method for a maneuvering target is evaluated. We choose the representative MTD, SCIFT, TDST, and ACCF-LVD algorithms as references. Complex zero-mean white Gaussian noise is added to radar echoes, and the SNR is set to be 5dB after compression. Figure 6a shows the target trajectory, and the result of MTD is given in Figure 6b. It is obvious that the MTD cannot integrate the target energy due to ignoring the LRM, QRM, and DFM. The velocity estimation and coherent integration results of the SCIFT are shown in Figure 6c,d, respectively. Unfortunately, the SCIFT is also invalid due to ignoring the target's acceleration.

(a)

(b)

(c)

(d)
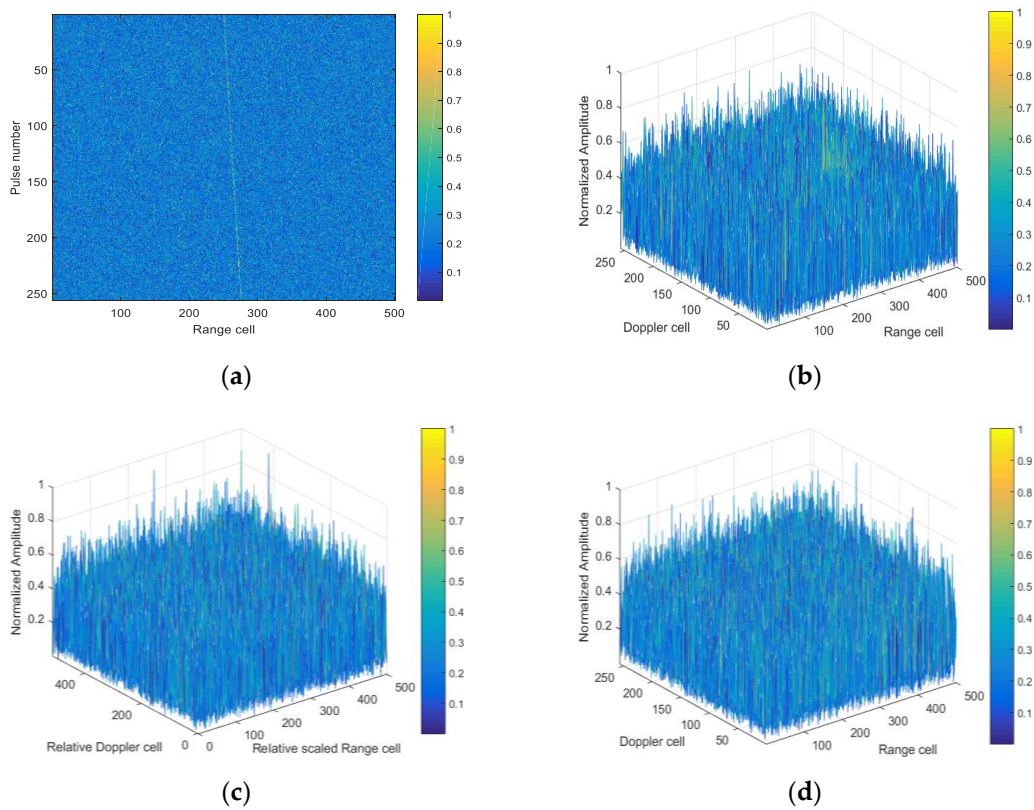
Figure 6. Coherent integration for a maneuvering target. (**a**) The result after pulse compression; (**b**) the integration result of moving target detection (MTD); (**c**) the velocity estimation result of the scaled inverse Fourier transform (SCIFT); (**d**) the integration result of the SCIFT.

Figure 7a shows the integration result of LVD, where no significant peak can be found. Thus, the ACCF-LVD cannot integrate target energy in such a low SNR, as shown in Figure 7b. Figure 7c–f give respectively the parameter estimation and integration results of the FD-SoPD and TDST. Although both algorithms can accurately estimate the target motion parameters and perform coherent accumulation, the proposed algorithm has much more advantages in computational efficiency and resources.

(a)

(b)

Figure 6. *Cont.*

(**c**)

(**d**)

(**e**)

(**f**)
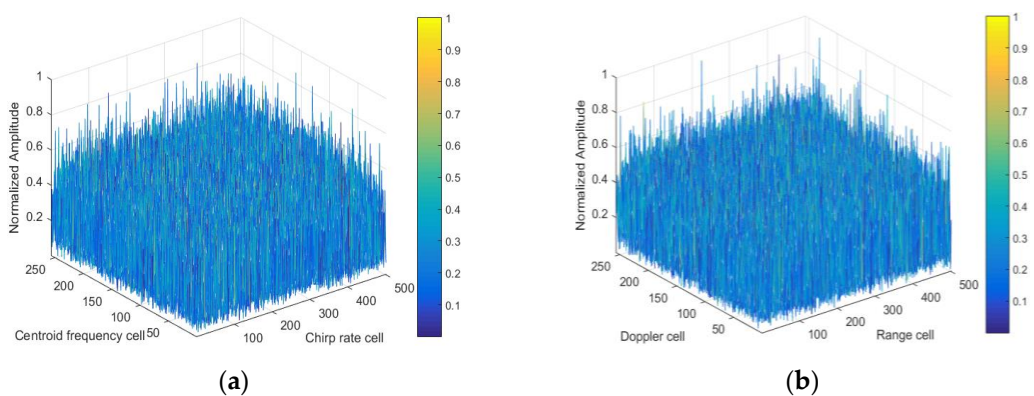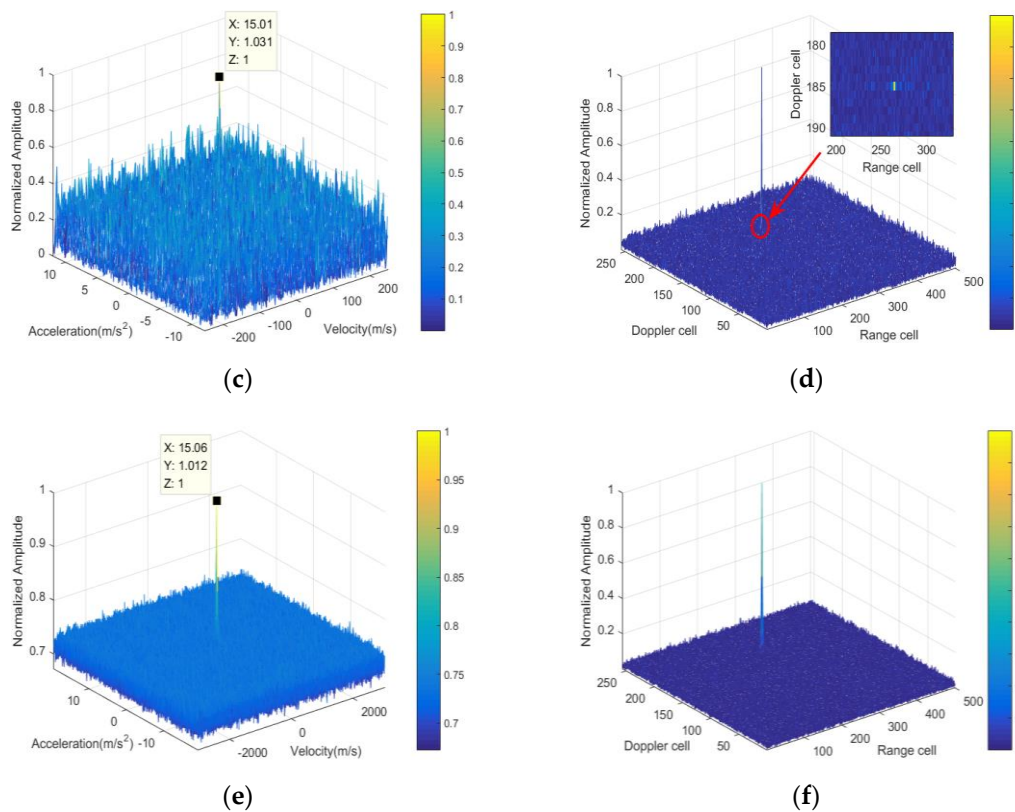
Figure 7. Integration performance comparison. (**a**) Parameter estimation result of LVD; (**b**) integration result of the ACCF-LVD; (**c**) parameter estimation result of the proposed algorithm; (**d**) integration result of the proposed algorithm; (**e**) parameter estimation result of the TDST; (**f**) integration result of the TDST.

Detailed results of parameter estimation and target detection are given in Table 3.

Table 3. Comparisons of simulated parameter estimation and target detection results.

	Initial Range (km)	Velocity (m/s)	Acceleration (m/s^2)	Detection Result
MTD	2.95	−1.65	-	No target
SCIFT	3.07	655.72	-	No target
ACCF-LVD	2.88	1043.84	11.386	No target
Proposed	3.00	15.01	1.031	Detected
TDST	3.00	15.06	1.012	Detected

5.2. Detection Performance

The detection ability of the above five algorithms is evaluated combined with the CFAR detector. Assume the radar data is contaminated by the zero-mean white Gaussian noise and input SNRs after pulse compression are set as [-20:1:20] dB. 200 trials are done for each SNR value. The false alarm rate is set as $P_{fa} = 10^{-6}$. Figure 8 shows the simulation result, where one can see that the MTD and SCIFT have the poorest detection probability due to ignoring the QRM or DFM. The adjacent cross-correlation function suffers more energy loss than the SoPD in the slow time domain [7]. Thus, the required SNR of FD-SoPD is about 4 dB less than ACCF-LVD. However, compared with TDST, the proposed algorithm suffers about 7 dB loss due to two-order bilinear transformation in SoPD. Considering the advantages of FD-SoPD, we can conclude that the proposed coherent detection algorithm achieves a good balance between the computational burden and detection ability.
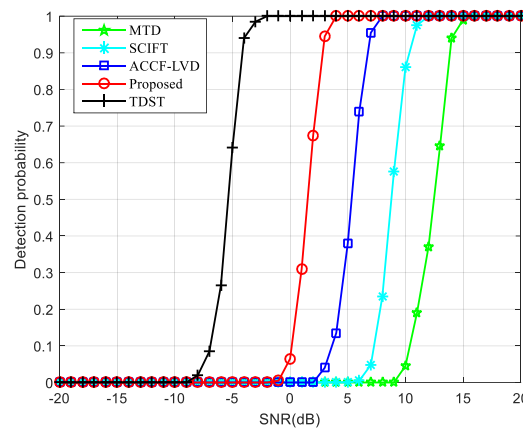
Figure 8. Detection probability of five algorithms.

5.3. Parameter Estimation Performance

We also evaluate the motion parameters estimation performance of FD-SoPD. The SNR after range compression varies from -15dB–20dB. The parameters for the radar and target are given in Table 2. two-hundred Monte Carlo simulations are performed for each SNR value. The root mean square error (RMSE) is utilized as a benchmark. The ACCF-LVD and TDST, which can estimate the velocity and acceleration of target, are selected for comparisons. Figure 9a,b show the RMSEs of the estimated velocity and acceleration. It can be seen that the TDST has the best estimation performance at the cost of huge computational burden. The performance of the proposed method is about 4dB better than those of ACCF-LVD on the input SNR threshold. However, compared with TDST, the FD-SoPD suffers from about 8dB SNR loss due to the constant delay in Equation (12). Overall, the proposed technique strikes a better balance between parameter estimation performance and computational cost.

(**a**)

(**b**)
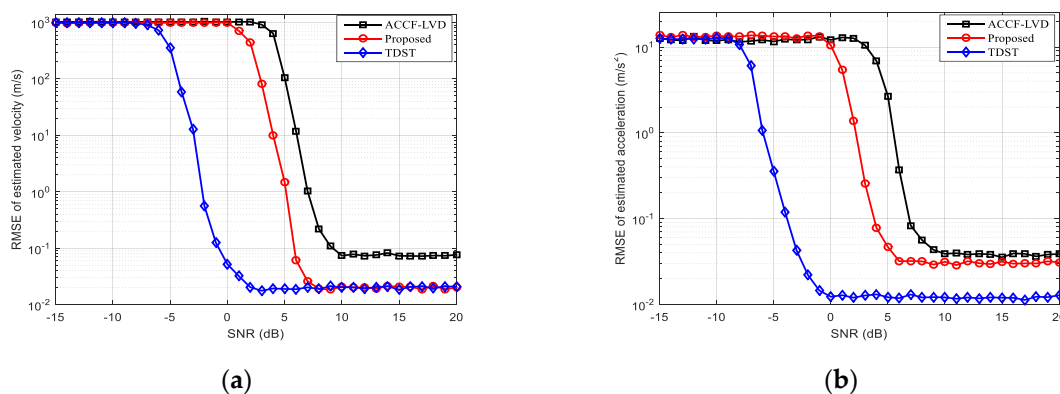
Figure 9. Motion parameters estimation performance of the three methods. (**a**) Estimation of the root mean square error (RMSE) of velocity; (**b**) estimation RMSE of acceleration.

5.4. Experimental Data Processing

In this subsection, we adopt the measured data of a DJI Phantom 3 commercial UAV to demonstrate the proposed FD-SoPD method. The data was collected in March 2017 by the National University of Defense Technology, Hunan, China. Figure 10a–c show the experimental scene, FMCW radar system, and radar antennas, respectively. Radar parameters are given in Table 4. Figure 10d shows the target trajectory after pulse compression, where the UAV moves across 7 range cells during the observation time. Figure 10e gives the parameter estimation result, where we could read the velocity and acceleration of the UAV, i.e., $\hat{v} = 1.217\,m/s$ and $\hat{a} = 0.2145\,m/s^2$. Finally, coherent integration of FD-SoPD can be obtained with the estimated velocity and acceleration,

as shown in Figure 10f. At the same time, the integration results of SCIFT and MTD are also given in Figure 10g,h. Due to ignoring the LRM, QRM, or DFM, the target energy is distributed in the range-Doppler domain. However, the proposed method can estimate the acceleration of the target accurately. Thus, a well-focused peak is obtained, which is beneficial to target detection. Detailed results of parameter estimation and coherent integration are given in Table 5.

(**a**)

(**b**)

(**c**)

(**d**)

Figure 9. *Cont.*

(e)

(f)

(g)

(h)
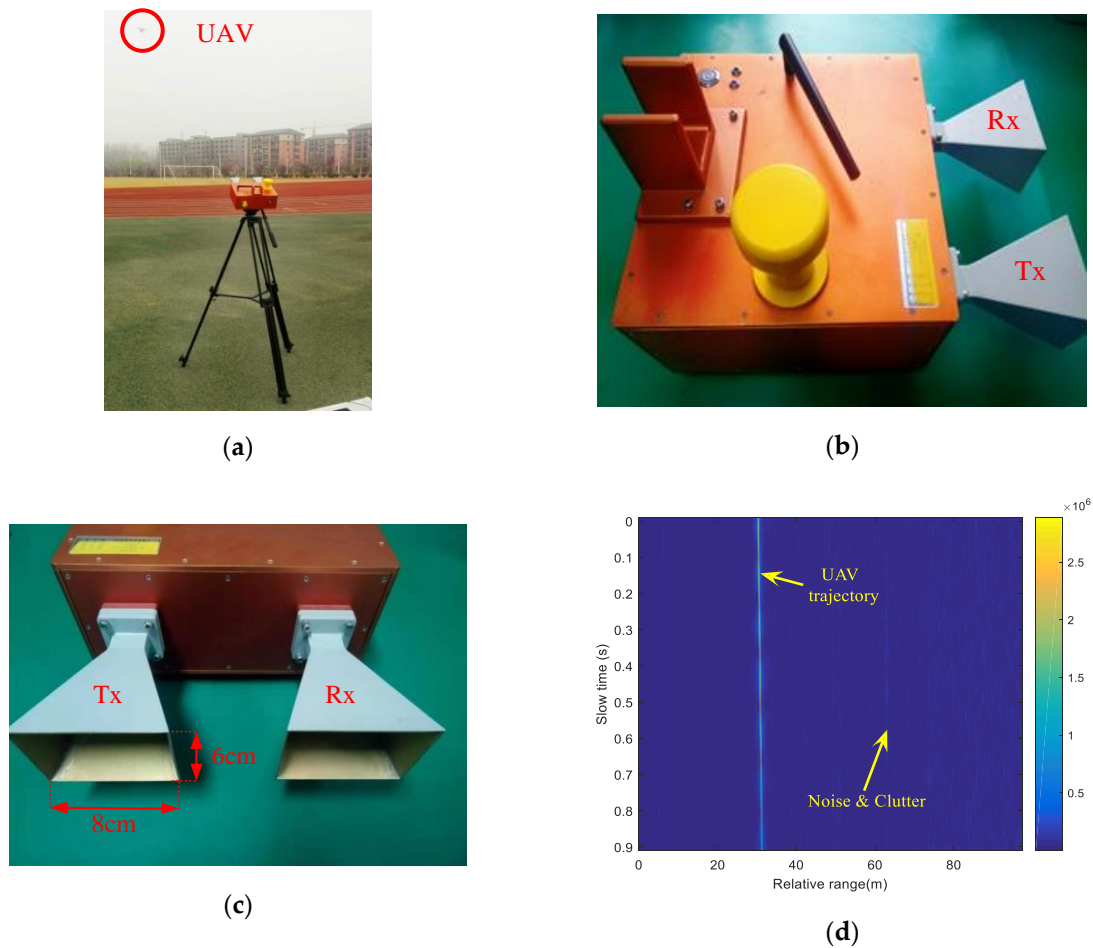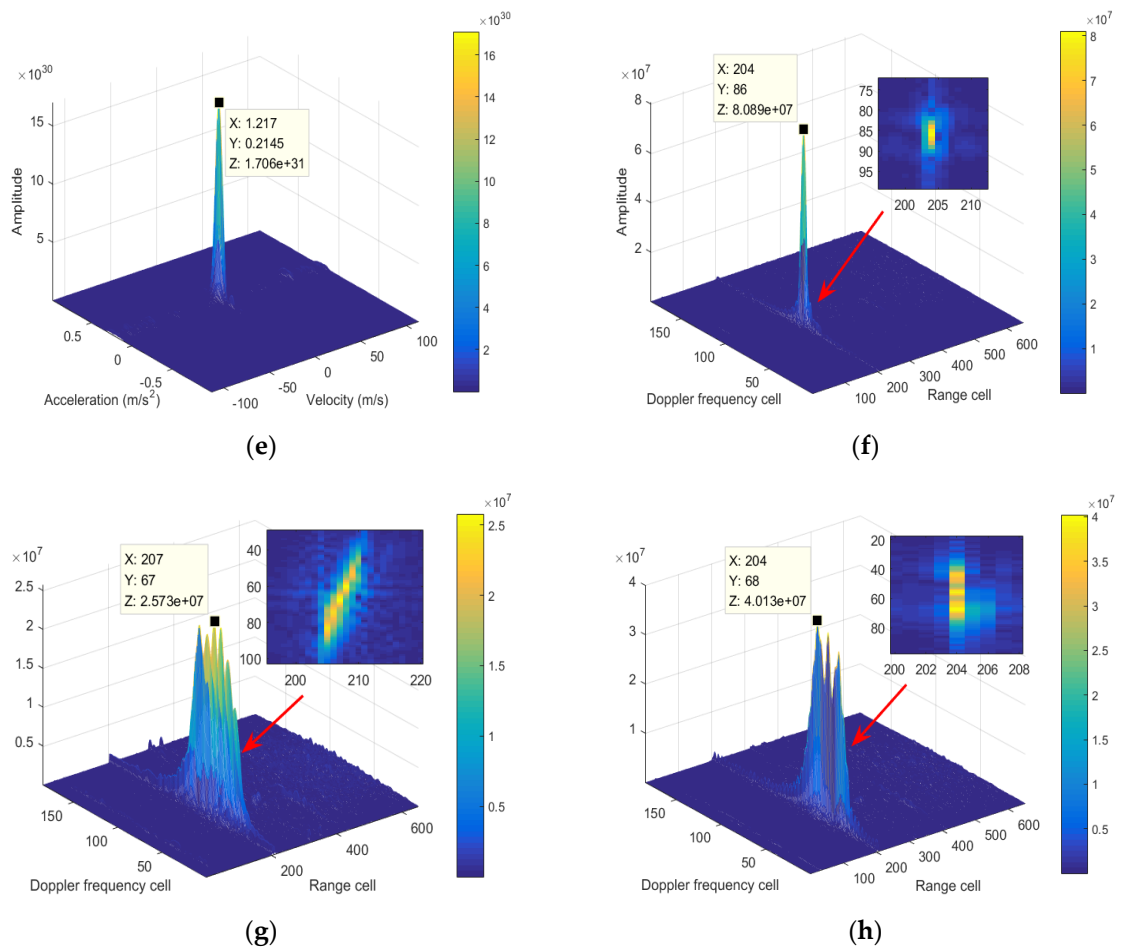
Figure 10. Experimental data processing results. (**a**) The experimental scene; (**b**) the FMCW radar system; (**c**) the radar antennas; (**d**) moving trajectory of the UAV; (**e**) parameter estimation result of FD-SoPD; (**f**) the coherent integration result of FD-SoPD; (**g**) the coherent integration result of the MTD; (**h**) the coherent integration result of the SCIFT.

Table 4. Frequency-modulated continuous-wave (FMCW) radar parameters.

Radar Parameter	Value	Radar Parameter	Value
Carrier frequency	9.5 GHz	PRF	50 Hz
Bandwidth	1 GHz	Sampling frequency	1 MHz
Pulse width	0.0102 s	Coherent time	0.92 s
Transmit power	25 dbm	Weight	7 kg
Radar length	35 cm	Radar width	24 cm
Radar height	20 cm	-	-

Table 5. Comparisons of experimental parameter estimation results.

	Range Cell	Velocity (m/s)	Acceleration (m/s^2)	Peak Value
MTD	207	−0.279	-	2.573×10^7
SCIFT	204	−0.283	-	4.013×10^7
FD-SoPD	204	1.217	0.2145	8.089×10^7

6. Conclusions

A frequency-domain second-order phase difference method is proposed to achieve coherent integration and parameter estimation. First, the FD-SoPD is performed to eliminate the QRM, DFM,

and Doppler ambiguity simultaneously. After that, parameter estimation and coherent integration are accomplished. Compared with ACCF-LVD, the FD-SoPD could obtain better detection performance with moderate computation complexity. Simulations and experimental data processing results demonstrate the effectiveness of the proposed algorithm.

Author Contributions: K.J., T.L. and Y.Z. conceived and designed the experiments; G.L. performed the experiments; Y.W. analyzed the data and contributed analysis tools; K.J. and Y.W. wrote the paper.

Appendix A

In this appendix, we will give the expressions of cross terms R_2-R_8. In order to simplify the expression form, we define

$$
\begin{aligned}
\varepsilon &= c/(f_r + f_c) \\
c_{i1} &= v_i \\
c_{i2} &= a_i/2 \\
A_i &= A_{f_r,i} rect\left(\frac{f_r}{B}\right) \exp\left(-j4\pi\frac{(f_r+f_c)}{c}r_i\right)
\end{aligned}
\tag{A1}
$$

Then the cross terms R_2-R_8 can be written as follows.

$$
R_2 = \sum_{\substack{i=1 \\ i\neq j}}^{K}\sum_{j=1}^{K}|A_i|^2|A_j|^2\exp\left\{j\frac{4\pi}{\varepsilon}\left[(c_{i1}-c_{j1})\tau + 2c_{i1}\tau_0 + 2(c_{i2}-c_{j2})t_m\tau + 4c_{i2}\tau_0 t_m\right]\right\}
\tag{A2}
$$

$$
\begin{aligned}
R_3 &= \sum_{p=1}^{K}|A_p|^2\exp\left[-j\frac{4\pi}{\varepsilon}(c_{p1}\tau + 2c_{p2}t_m\tau)\right] \times \sum_{\substack{k=1 \\ k\neq l}}^{K}\sum_{l=1}^{K}A_k^*A_l \\
&\times \exp\left\{j\frac{4\pi}{\varepsilon}\left[c_{k1}\left(t_m + \frac{\tau}{2} + \tau_0\right) + c_{k2}\left(t_m + \frac{\tau}{2} + \tau_0\right)^2 - c_{l1}\left(t_m - \frac{\tau}{2} - \tau_0\right) + c_{l2}\left(t_m - \frac{\tau}{2} - \tau_0\right)^2\right]\right\}
\end{aligned}
\tag{A3}
$$

$$
\begin{aligned}
R_4 &= \sum_{q=1}^{K}|A_q|^2\exp\left[j\frac{4\pi}{\varepsilon}(c_{q1}\tau + 2c_{q2}t_m\tau + 4c_{q2}t_m\tau_0)\right] \times \sum_{\substack{i=1 \\ i\neq j}}^{K}\sum_{j=1}^{K}A_iA_j^* \\
&\exp\left\{-j\frac{4\pi}{\varepsilon}\left[c_{i1}\left(t_m + \frac{\tau}{2}\right) + c_{i2}\left(t_m + \frac{\tau}{2}\right)^2 - c_{j1}\left(t_m - \frac{\tau}{2}\right) - c_{j2}\left(t_m - \frac{\tau}{2}\right)^2\right]\right\}
\end{aligned}
\tag{A4}
$$

$$
\begin{aligned}
R_5 &= \sum_{\substack{i=1 \\ i\neq j}}^{K}\sum_{j=1}^{K}A_iA_j^*\exp\left\{-j\frac{4\pi}{\varepsilon}\left[c_{i1}\left(t_m + \frac{\tau}{2}\right) + c_{i2}(t_m+)^2\right]\right\} \\
&\times \exp\left\{-j\frac{4\pi}{\varepsilon}\left[c_{j1}\left(t_m - \frac{\tau}{2}\right) + c_{j2}\left(t_m - \frac{\tau}{2}\right)^2\right]\right\} \\
&\times \sum_{\substack{k=1 \\ k\neq l}}^{K}\sum_{l=1}^{K}A_k^*A_l\exp\left\{j\frac{4\pi}{\varepsilon}\left[c_{k1}\left(t_m + \frac{\tau}{2} + \tau_0\right) + c_{k2}\left(t_m + \frac{\tau}{2} + \tau_0\right)^2\right]\right\} \\
&\times \exp\left\{-j\frac{4\pi}{\varepsilon}\left[c_{l1}\left(t_m - \frac{\tau}{2} - \tau_0\right) + c_{l2}\left(t_m - \frac{\tau}{2} - \tau_0\right)^2\right]\right\}
\end{aligned}
\tag{A5}
$$

$$
\begin{aligned}
R_6 &= \sum_{\substack{i=1 \\ i\neq j}}^{K}\sum_{j=1}^{K}|A_i|^2|A_j|^2\exp\left\{j\frac{4\pi}{\varepsilon}\left[(c_{i1}+c_{j1})\tau_0 + (c_{i2}-c_{j2})\tau_0^2\right]\right\} \\
&\times \exp\left\{j\frac{4\pi}{\varepsilon}\left[2(c_{i2}+c_{j2})\tau_0 t_m + (c_{i2}-c_{j2})\tau_0\tau\right]\right\}
\end{aligned}
\tag{A6}
$$

$$R_7 = \sum_{\substack{i=1 \\ i \neq j}}^{K} \sum_{j=1}^{K} A_i A_j^* \exp\left\{-j\frac{4\pi}{\varepsilon}\left[c_{i1}\left(t_m + \frac{\tau}{2}\right) + c_{i2}\left(t_m + \frac{\tau}{2}\right)^2\right]\right\}$$

$$\times \exp\left\{j\frac{4\pi}{\varepsilon}\left[c_{j1}\left(t_m - \frac{\tau}{2}\right) + c_{j2}\left(t_m - \frac{\tau}{2}\right)^2\right]\right\}$$

$$\times \sum_{\substack{k=1 \\ k \neq i, l \neq j, k \neq l}}^{K} \sum_{l=1}^{K} A_k^* A_l \exp\left\{j\frac{4\pi}{\varepsilon}\left[c_{k1}\left(t_m + \frac{\tau}{2} + \tau_0\right) + c_{k2}\left(t_m + \frac{\tau}{2} + \tau_0\right)^2\right]\right\}$$

$$\times \exp\left\{-j\frac{4\pi}{\varepsilon}\left[c_{l1}\left(t_m - \frac{\tau}{2} - \tau_0\right) + c_{l2}\left(t_m - \frac{\tau}{2} - \tau_0\right)^2\right]\right\} \tag{A7}$$

$$R_8 = \sum_{\substack{i=1 \\ i \neq j}}^{K} \sum_{j=1}^{K} A_i A_j^* \exp\left\{-j\frac{4\pi}{\varepsilon}\left[c_{i1}\left(t_m + \frac{\tau}{2}\right) + c_{i2}\left(t_m + \frac{\tau}{2}\right)^2 - c_{j1}\left(t_m - \frac{\tau}{2}\right) - c_{j2}\left(t_m - \frac{\tau}{2}\right)^2\right]\right\}$$

$$\times \sum_{\substack{k=1 \\ k=i, l \neq j, k \neq l}}^{K} \sum_{l=1}^{K} A_k^* A_l \exp\left\{j\frac{4\pi}{\varepsilon}\left[c_{k1}\left(t_m + \frac{\tau}{2} + \tau_0\right) + c_{k2}\left(t_m + \frac{\tau}{2} + \tau_0\right)^2 - c_{l1}\left(t_m - \frac{\tau}{2} - \tau_0\right) - c_{l2}\left(t_m - \frac{\tau}{2} - \tau_0\right)^2\right]\right\}$$

$$+ \sum_{\substack{i=1 \\ i \neq j}}^{K} \sum_{j=1}^{K} A_i A_j^* \exp\left\{-j\frac{4\pi}{\varepsilon}\left[c_{i1}\left(t_m + \frac{\tau}{2}\right) + c_{i2}\left(t_m + \frac{\tau}{2}\right)^2 - c_{j1}\left(t_m - \frac{\tau}{2}\right) - c_{j2}\left(t_m - \frac{\tau}{2}\right)^2\right]\right\}$$

$$\times \sum_{\substack{k=1 \\ k \neq i, l = j, k \neq l}}^{K} \sum_{l=1}^{K} A_k^* A_l \exp\left\{j\frac{4\pi}{\varepsilon}\left[c_{k1}\left(t_m + \frac{\tau}{2} + \tau_0\right) + c_{k2}\left(t_m + \frac{\tau}{2} + \tau_0\right)^2 - c_{l1}\left(t_m - \frac{\tau}{2} - \tau_0\right) - c_{l2}\left(t_m - \frac{\tau}{2} - \tau_0\right)^2\right]\right\} \tag{A8}$$

References

1. Huang, P.H.; Liao, G.S.; Yang, Z.Z.; Xia, X.G.; Ma, J.T.; Ma, J.T. Long-Time Coherent Integration for Weak Maneuvering Target Detection and High-Order Motion Parameter Estimation Based on Keystone Transform. *IEEE Trans. Signal Process.* **2016**, *64*, 4013–4026. [CrossRef]
2. Suo, P.C.; Tao, S.; Tao, R.; Nan, Z. Detection of high-speed and accelerated target based on the linear frequency modulation radar. *IET Radar Sonar Navig.* **2014**, *8*, 37–47. [CrossRef]
3. Zhu, S.Q.; Liao, G.S.; Yang, D.; Tao, H.H. A New Method for Radar High-Speed Maneuvering Weak Target Detection and Imaging. *IEEE Geosci. Remote Sens. Lett.* **2014**, *11*, 1175–1179.
4. Li, X.L.; Sun, Z.; Yi, W.; Cui, G.L.; Kong, L.J.; Yang, X.B. Computationally efficient coherent detection and parameter estimation algorithm for maneuvering target. *Signal Process.* **2018**, *155*, 130–142. [CrossRef]
5. Li, X.L.; Cui, G.L.; Yi, W.; Kong, L.J. Fast coherent integration for maneuvering target with high-order range migration via TRT-SKT-LVD. *IEEE Trans. Aerospace Electr. Syst.* **2016**, *52*, 2803–2814. [CrossRef]
6. Wu, W.; Wang, G.H.; Sun, J.P. Polynomial Radon-Polynomial Fourier Transform for Near Space Hypersonic Maneuvering Target Detection. *IEEE Trans. Aerospace Electr. Syst.* **2018**, *54*, 1306–1322. [CrossRef]
7. Zhang, J.C.; Su, T.; Zheng, J.B.; He, X.H. Novel Fast Coherent Detection Algorithm for Radar Maneuvering Target with Jerk Motion. *IEEE J. Sel. Top. Appl. Earth Observ. Remote Sens.* **2017**, *10*, 1792–1803. [CrossRef]
8. Lao, G.C.; Yin, C.B.; Ye, W.; Sun, Y.; Li, G.J. An SAR-ISAR Hybrid Imaging Method for Ship Targets Based on FDE-AJTF Decomposition. *Electronics* **2018**, *7*, 46. [CrossRef]
9. Lv, Y.K.; Wu, Y.H.; Wang, H.Y.; Qiu, L.; Jiang, J.W.; Sun, Y. An Inverse Synthetic Aperture Ladar Imaging Algorithm of Maneuvering Target Based on Integral Cubic Phase Function-Fractional Fourier Transform. *Electronics* **2018**, *7*, 148. [CrossRef]
10. Lazarov, A.; Minchev, C. ISAR Geometry, Signal Model, and Image Processing Algorithms. *IET Radar Sonar Navig.* **2017**, *11*, 1425–1434. [CrossRef]
11. Li, X.L.; Kong, L.J.; Cui, G.L.; Yi, W. A low complexity coherent integration method for maneuvering target detection. *Dig. Signal Process.* **2016**, *49*, 137–147. [CrossRef]
12. Rao, X.; Tao, H.H.; Su, J.; Xie, J.; Zhang, X.Y. Detection of Constant Radial Acceleration Weak Target via IAR-FRFT. *IEEE Trans. Aerospace Electr. Syst.* **2015**, *51*, 3242–3253. [CrossRef]
13. Xu, J.; Yu, J.; Peng, Y.N.; Xia, X.G. Radon-Fourier Transform for Radar Target Detection, I: Generalized Doppler Filter Bank. *IEEE Trans. Aerospace Electr. Syst.* **2011**, *47*, 1186–1202. [CrossRef]
14. Zhu, D.Y.; Li, Y.; Zhu, Z.D. A Keystone Transform Without Interpolation for SAR Ground Moving-Target Imaging. *IEEE Geosci. Remote Sens. Lett.* **2007**, *4*, 18–22. [CrossRef]

15. Sun, G.C.; Xing, M.D.; Xia, X.G.; Wu, Y.R.; Bao, Z. Robust Ground Moving-Target Imaging Using Deramp–Keystone Processing. *IEEE Trans. Geosci. Remote Sens.* **2013**, *51*, 966–982. [CrossRef]

16. Zheng, J.B.; Su, T.; Zhu, W.T.; He, X.H.; Liu, Q.H. Radar High-Speed Target Detection Based on the Scaled Inverse Fourier Transform. *IEEE J. Sel. Top. Appl. Earth Observ. Remote Sens.* **2015**, *8*, 1108–1119. [CrossRef]

17. Niu, Z.Y.; Zheng, J.B.; Su, T.; Zhang, J.C. Fast implementation of scaled inverse Fourier transform for high-speed radar target detection. *Electr. Lett.* **2017**, *53*, 1142–1144. [CrossRef]

18. Zheng, J.B.; Su, T.; Liu, H.W.; Liao, G.S.; Liu, Z.; Liu, Q.H. Radar High-Speed Target Detection Based on the Frequency-Domain Deramp-Keystone Transform. *IEEE J. Sel. Top. Appl. Earth Observ. Remote Sens.* **2016**, *9*, 285–294. [CrossRef]

19. Sun, Z.; Li, X.L.; Yi, W.; Cui, G.L.; Kong, L.J. A Coherent Detection and Velocity Estimation Algorithm for the High-Speed Target Based on the Modified Location Rotation Transform. *IEEE J. Sel. Top. Appl. Earth Observ. Remote Sens.* **2018**, *11*, 2346–2361. [CrossRef]

20. Xu, J.; Yu, J.; Peng, Y.N.; Xia, X.G. Radon-Fourier Transform for Radar Target Detection (II): Blind Speed Sidelobe Suppression. *IEEE Trans. Aerospace Electr. Syst.* **2011**, *47*, 2473–2489. [CrossRef]

21. Xu, J.; Xia, X.G.; Peng, S.B.; Yu, J.; Peng, Y.N.; Qian, L.C. Radar Maneuvering Target Motion Estimation Based on Generalized Radon-Fourier Transform. *IEEE Trans. Signal Process.* **2012**, *60*, 6190–6201.

22. Chen, X.L.; Guan, J.; Liu, N.B.; He, Y. Maneuvering Target Detection via Radon-Fractional Fourier Transform-Based Long-Time Coherent Integration. *IEEE Trans. Signal Process.* **2014**, *62*, 939–953. [CrossRef]

23. Li, X.L.; Cui, G.L.; Yi, W.; Kong, L.J. Coherent Integration for Maneuvering Target Detection Based on Radon-Lv's Distribution. *IEEE Signal Process. Lett.* **2015**, *22*, 1467–1471. [CrossRef]

24. Lv, X.L.; Bi, G.A.; Wan, C.R.; Xing, M.D. Lv's Distribution: Principle, Implementation, Properties, and Performance. *IEEE Trans. Signal Process.* **2011**, *59*, 3576–3591. [CrossRef]

25. Lv, X.L.; Xing, M.D.; Zhang, S.H.; Bao, Z. Keystone transformation of the Wigner-Ville distribution for analysis of multicomponent LFM signals. *Signal Process.* **2009**, *59*, 791–806. [CrossRef]

26. Zheng, J.B.; Liu, H.W.; Liu, Q.H. Parameterized Centroid Frequency-Chirp Rate Distribution for LFM Signal Analysis and Mechanisms of Constant Delay Introduction. *IEEE Trans. Signal Process.* **2017**, *65*, 6435–6447. [CrossRef]

27. Kirkland, D. Imaging moving targets using the second-order keystone transform. *IET Radar Sonar Navig.* **2011**, *5*, 902–910. [CrossRef]

28. Li, G.; Xia, X.G.; Peng, Y.N. Doppler Keystone Transform: An Approach Suitable for Parallel Implementation of SAR Moving Target Imaging. *IEEE Geosci. Remote Sens. Lett.* **2008**, *5*, 573–577. [CrossRef]

29. Li, X.L.; Cui, G.L.; Yi, W.; Kong, L.J. Manoeuvring target detection based on keystone transform and Lv's distribution. *IET Radar Sonar Navig.* **2016**, *10*, 1234–1242. [CrossRef]

30. Li, X.L.; Cui, G.L.; Yi, W.; Kong, L.J. A Fast Maneuvering Target Motion Parameters Estimation Algorithm Based on ACCF. *IEEE Signal Process. Lett.* **2015**, *22*, 270–274. [CrossRef]

31. Li, X.L.; Cui, G.L.; Kong, L.J.; Yi, W. Fast Non-Searching Method for Maneuvering Target Detection and Motion Parameters Estimation. *IEEE Trans. Signal Process.* **2016**, *64*, 2232–2244. [CrossRef]

32. Li, X.L.; Cui, G.L.; Yi, W.; Kong, L.J. Radar Maneuvering Target Detection and Motion Parameter Estimation Based on TRT-SGRFT. *Signal Process.* **2017**, *133*, 107–116. [CrossRef]

33. He, X.P.; Liao, G.S.; Zhu, S.Q.; Xu, J.W.; Guo, Y.F.; Wei, J.Q. Fast Non-Searching Method for Ground Moving Target Refocusing and Motion Parameters Estimation. *Digital Signal Process.* **2018**, *79*, 152–163. [CrossRef]

34. Zheng, J.B.; Liu, H.W.; Liu, J.; Du, X.L.; Liu, Q.H. Radar High-Speed Maneuvering Target Detection Based on Three-Dimensional Scaled Transform. *IEEE J. Sel. Top. Appl. Earth Observ. Remote Sens.* **2018**, *11*, 2821–2833. [CrossRef]

35. Zheng, J.B.; Su, T.; Zhang, L.; Zhu, W.T.; Liu, Q.H. ISAR Imaging of Targets with Complex Motion Based on the Chirp Rate–Quadratic Chirp Rate Distribution. *IEEE Trans. Geosci. Remote Sens.* **2014**, *52*, 7276–7289. [CrossRef]

36. Guida, M.; Longo, M.; Lops, M. Biparametric CFAR procedures for lognormal clutter. *IEEE Trans. Aerospace Electr. Syst.* **1993**, *29*, 798–809. [CrossRef]